

The $E \times B$ staircase as the self-organization in the tokamak avalanche plasma

Minjun J. Choi¹, Jae-Min Kwon¹, Lei Qi¹, P. H. Diamond², T. S. Hahm³, Hogun Jhang¹, Juhyung Kim¹, Michael Leconte¹, Hyun-Seok Kim¹, Jisung Kang¹, Byoung-Ho Park¹, Jinil Chung¹, Jaehyun Lee¹, Minho Kim¹, Gunsu S. Yun⁴, Y. U. Nam¹, Jaewook Kim¹, Won-Ha Ko¹, K. D. Lee¹, J. W. Juhn¹ and the KSTAR team

¹ Korea Institute of Fusion Energy, Daejeon 34133, Republic of Korea

² University of California, San Diego, La Jolla, California 92093-0424, U.S.A.

³ Seoul National University, Seoul 08826, Republic of Korea

⁴ Pohang University of Science and Technology, Pohang, Gyeongbuk 37673, Republic of Korea

E-mail: mjchoi@kfe.re.kr

Abstract.

The self-organization is one of the most interesting phenomena in the non-equilibrium complex system, generating ordered structures of various size and duration. The physical mechanism and characteristics of the self-organization phenomena are closely related with the underlying transport mechanism and characteristics. In tokamak plasmas, globally self-organized mini transport barriers, the $E \times B$ staircase, are observed in the particular transport regime where non-diffusive flux propagation events, the avalanche, are prevalent. Various models have been suggested to understand this globally self-organized state of transport barriers and its relation with the avalanche transport. While intensive simulation studies have been conducted to advance the understanding, the experimental researches have been mostly limited to the demonstration of their existence. In this work, detail characteristics of both the avalanche transport and the $E \times B$ staircase in KSTAR plasmas are analyzed. The avalanche transport is found to have strong influences on the formation and statistics of the $E \times B$ staircase. In addition, a perspective to consider the $E \times B$ staircase as the self-organization near an non-equilibrium critical state is discussed to understand its dynamics and statistics and the relation with the stationary internal transport barrier.

1. Introduction

Tokamak plasmas can be considered one of the thermodynamic non-equilibrium complex systems [1]. The central region of plasmas is heated by external heating and current drive (via the Joule effect), and the edge region of plasmas is attached to any form of heat sinks such as a limiter, a divertor and a radiation belt. With these constraints, plasmas reach a stationary non-equilibrium state characterized by the finite heat flux (breaking of detailed balance) and temperature gradient between the hot center and the cold edge. Gradients in temperature, plasma density or current density serve as a drive for various plasma instabilities which can carry the significant amount of flux. In a particular regime where macroscopic (\sim the plasma radius a) MHD instabilities, which can be described by a relatively simple equation, are suppressed, microscopic (\sim the gyro-radius ρ) instabilities such as drift wave instabilities matter in plasma transport. Then, plasmas would exhibit features of a complex system composed of the great number of interacting elements. Microscopic instabilities in tokamak plasmas, or simply plasma turbulence, can interact in various ways beyond their microscopic auto-correlation lengths [2, 3].

The most interesting feature of complex systems is the self-organization phenomena generating ordered structures of various size and duration [4, 5]. Distributions of characteristics of self-organized structures are rarely normal, and their complicated dynamics and long time patterns are sensitive to the initial random microscopic condition.

One of the well known examples may be the Rayleigh-Bénard convection cells observed in a layer of fluid between two horizontal parallel plates kept at different temperature ($\Delta T = T_{\text{bottom}} - T_{\text{top}} > 0$) [1, 4]. When the temperature difference is small, the conductive state with the homogenous velocity field is stable. However, it becomes unstable and convective cells start to form when ΔT is increased above some critical value ΔT_c (but not increased too much), i.e. the Rayleigh-Bénard instability [1]. Eventually, the system reaches a non-equilibrium stationary state with a macroscopic ordered pattern of convection cells after complicated coalescence and splitting of convective cells.

The physical meaning of the $\Delta T > \Delta T_c$ condition for the Rayleigh-Bénard instability lies in the competition between conductive and convective transport efficiencies in the system [1]. Since conduction is a diffusive process, the relevant time (τ_{cond}) is simply the diffusion time (the system size²/diffusivity). The convective time (τ_{conv}) can be taken as the system size divided by the convection speed where the convection speed is obtained by balancing the buoyancy force (originated from the thermal expansion by the local temperature increase) and the viscous force. Then, the ratio between two times ($\tau_{\text{cond}}/\tau_{\text{conv}}$) turns out to be the Rayleigh number $\text{Ra} = \text{Ra}(\Delta T)$ [1]. The rephrased condition $\text{Ra}(\Delta T) > \text{Ra}(\Delta T_c)$ means that the Rayleigh-Bénard cells appear when the convective transport is sufficiently more efficient than the conductive transport, overcoming the viscous force.

The recent observation in tokamak plasmas, a macroscopic ordered pattern of zonal flows, or the $E \times B$ staircase [6, 7], can be another example of the self-organization phenomena in complex non-equilibrium systems. The zonal flow in tokamak plasmas is the self-organized flow structure out of turbulent fluctuation bath, self-regulating the turbulent transport [8]. While it had been sometimes described by models which span only a few turbulence correlation length, it was observed that multiple zonal flows at different radial locations over the entire plasma arise together with an apparent correlation [6, 7]. They act like mini permeable transport barriers and generate a staircase-like pressure profile corrugation [9, 10, 11]. Their observations have been reported in many gyrokinetic simulations [6, 12, 13, 14, 15, 16, 17] and experiments [18, 19, 9, 10, 20, 11]. Unfortunately, the physics of the $E \times B$ staircase, especially their long range correlation, has not been understood clearly yet, though various models were suggested [21, 22, 23, 24, 15, 25, 26, 27, 28].

Although there may be no universal laws for various self-organized structures in complex non-equilibrium systems, lessons can be learned by comparing observations in different systems [5]. The Rayleigh-Bénard cells and the $E \times B$ staircase actually share interesting properties: (1) symmetry breaking from a homogeneous disordered state to an inhomogeneous ordered state, (2) sensitivity to the initial fluctuations but resilience or persistence against the perturbation after formation and (3) the macroscopic correlation length. Since the critical condition for the Rayleigh-Bénard instability is associated with the change of the dominant transport mechanism to non-diffusive one, it would be interesting to ask how the physics of the $E \times B$ staircase relates to the underlying transport characteristics.

The investigation based on intense gyrokinetic simulations revealed one important clue that the $E \times B$ staircase is most frequently observed near the marginal condition [7] in which the non-diffusive avalanche transport becomes important [29]. Here, the avalanche transport means a near ballistic flux propagation event [2] often observed in both simulations [30, 31, 32, 33] and experiments [34, 35, 36, 9, 37, 38]. The near marginal regime can be characterized using the Kubo number $K \equiv \tau_{\text{rsd}}/\tau_{\text{int}}$, defined by the ratio between the particle's residing time (τ_{rsd}) on a turbulent eddy and the particle's interaction time (τ_{int}) with a turbulent eddy [39]. $K < 1$ means that the transport would be a diffusive process by many kicks across turbulent eddies, and $K > 1$ means that the transport would be an excursion over the turbulent eddy structure beyond the typical eddy correlation length. The near marginal regime corresponds to $K > 1$, dominated by the long range avalanche transport [39]. In addition to the avalanche transport, the phase space density granulation can be also important for the zonal flow and transport for the $K > 1$ near marginal regime [40, 41]. The avalanche transport and/or the phase space density granulation may be related to the $E \times B$ staircase physics, but more researches are required to clarify their relation.

While in simulation researches various characteristics of the $E \times B$ staircase have been analyzed to understand their relation with the avalanche transport [7, 15, 42], the experimental researches have been mostly limited to demonstrating existence of such

a structure. The identification of the $E \times B$ staircase, or globally self-organized mini transport barriers, in plasma experiments was done indirectly due to the difficulty to measure the fine scale poloidal flow variation directly. In Tore Supra [18, 19] and HL-2A [11], the radial variation of the turbulence correlation length and the corresponding turbulence eddy tilting are provided as evidences for the shear flow layers, the $E \times B$ staircase. In TJ-II [43], W7-X [44] and JET [20], the radial transfer of information in fluctuation is analyzed to identify the radially localized minor barriers, or trapping regions, where the information is trapped relatively longer [20]. In KSTAR [9], DIII-D [10], and HL-2A [11], the staircase-like corrugation of temperature/density profiles are provided, demonstrating the existence of the long range correlated transport barriers. It is noteworthy that the co-existence of the avalanche transport and the $E \times B$ staircase was only reported in the KSTAR experiment [9].

In this work, various characteristics of the avalanche transport and the $E \times B$ staircase observed in KSTAR have been analyzed to understand their relation. The rest of this paper is organized as follows. In Section 2, it will be explained how the avalanche transport and the $E \times B$ staircase are identified and their characteristics are measured in KSTAR experiments. In Sections 3 (the avalanche transport) and 4 (the $E \times B$ staircase), measurements and analyses of their dynamics and statistics will be provided, respectively. Conclusion and discussion will follow in Section 5. Besides the intellectual interest on this intricate phenomenon, the improved understanding of the near marginal regime transport would be critical to advance the current predictive capability of tokamak plasma confinement. The near marginal regime is shown to be a good test bed for suspicious assumptions used in the reduced models [39].

2. The avalanche transport, the $E \times B$ staircase, and the KSTAR experiment

2.1. The avalanche transport

In this paper, the avalanche means the transport event of various size, involving ballistic propagations of the down-gradient electron temperature bump ($\delta T_e > 0$) and the up-gradient void ($\delta T_e < 0$), but not involving a significant magnetic fluctuation [9]. Fig. 1(a) shows the filtered (for larger avalanches) T_e time traces measured at different radial locations in the KSTAR plasmas (major radius $R_0 = 1.8$ m and minor radius $a = 0.5$ m [45]). The large avalanches whose bumps propagate to the plasma edge (indicated by gray dashed lines in Fig. 1(a)) have a propagation speed of ≤ 100 m/s. They are relatively rare, and the smaller events, which are probably dissipated by the finite diffusive transport and buried by noises, are more frequent (see Section 3 for detail analyses). They seem to preserve the join reflection symmetry [29] against the avalanche initiation location $R = R_{av}$ (see Fig. 1(d) for the illustration), and would correspond to electrostatic transport events.

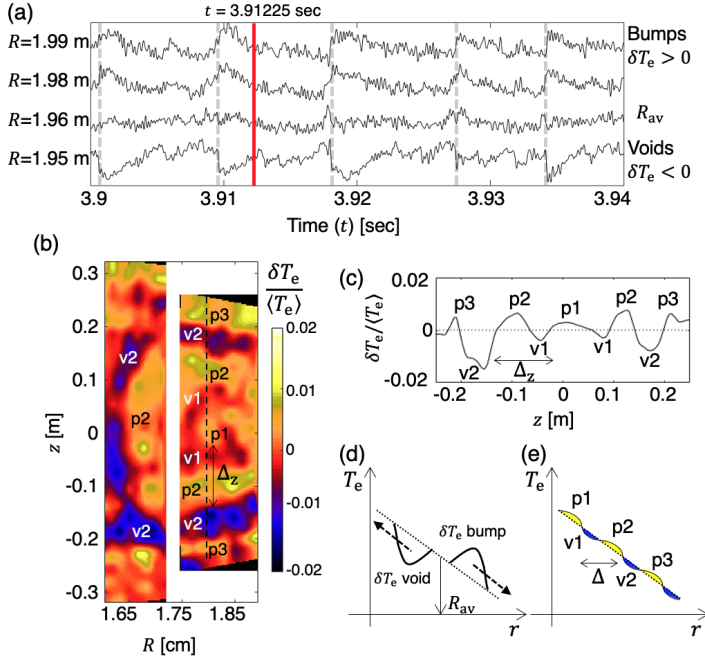


Figure 1. (a) T_e time traces measured at different radial locations (y-axis). Bumps and voids of various size avalanches are generated near R_{av} in the plasma core region. Large size avalanches whose bumps propagate to the plasma edge are indicated by dashed lines. (b) Two-dimensional measurement of $\delta T_e / \langle T_e \rangle$ at 3.91225 sec in between large avalanches. Jet-like patterns in the $\delta T_e / \langle T_e \rangle$ image correspond to a staircase-like T_e corrugation (the $E \times B$ staircase) and letters ‘p’s and ‘v’s represent peaks and valleys of $\delta T_e / \langle T_e \rangle$, respectively. (c) The vertical cut of $\delta T_e / \langle T_e \rangle$ measurement along the plasma center. Δ_z indicates the vertical tread width of the staircase. (d) The illustration of the avalanche, preserving the joint reflection symmetry. (e) The illustration of a staircase-like T_e profile corrugation with the radial tread width Δ by the $E \times B$ staircase. Dotted lines in illustrations represent the average temperature $\langle T_e \rangle$ profile.

2.2. The $E \times B$ staircase

The $E \times B$ staircase means the globally self-organized transport barriers identified by a long range staircase-like electron temperature (T_e) corrugation in the KSTAR avalanche plasmas [9]. Fig. 1(b) shows an example of the T_e corrugation in the poloidal cross section of the KSTAR plasma at 3.91225 sec (red line in Fig. 1(a), away from the large avalanches). Its vertical cut is plotted in Fig. 1(c). The T_e corrugation appears as poloidally symmetric jet-like patterns in the $\delta T_e / \langle T_e \rangle$ image, and its peaks and valleys are indicated by ‘p’s and ‘v’s letters (see Fig. 1(e) for the illustration). They can drift radially and, the lifetime of this T_e corrugation was about 1 msec and its vertical step width was $\Delta_z \approx 10.8$ cm [9] (see Section 4 for detail analyses). This temperature corrugation reflects the existence of the mini transport barriers confining the avalanche transport within the meso-scale step width [9].

The comparison of propagations of the large avalanche without and with the temperature corrugation demonstrates its avalanche stopping capability [12] and

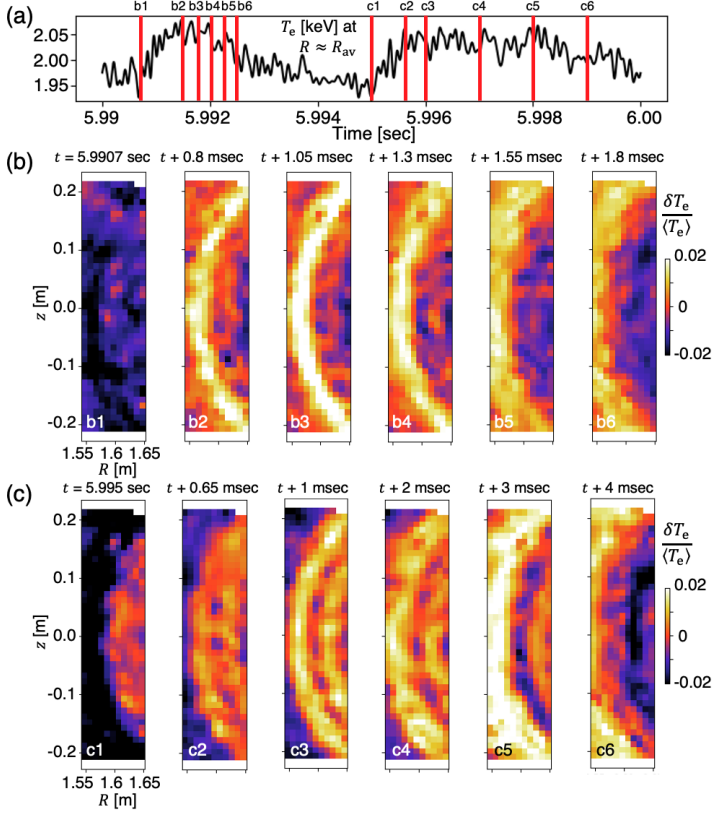


Figure 2. (a) The T_e time trace at $R \approx R_{av}$. Measurement times of $\delta T_e / \langle T_e \rangle$ images shown in (b) and (c) are indicated by red lines and letters 'b's and 'c's, respectively. $\delta T_e / \langle T_e \rangle$ images along time (t) during the large avalanche (b) without and (c) with the $E \times B$ staircase.

partially justifies its naming as the $E \times B$ staircase in this paper (see also Section 4.2). Figs. 2(b) and 2(c) show $\delta T_e / \langle T_e \rangle$ images for propagations of bumps and voids of the large avalanche without and with the temperature corrugation, respectively. They are observed consecutively, and their bumps detected in the local T_e time trace near $R \approx R_{av}$ are shown in Fig. 2(a) with indication of times of the images (red lines). In Fig. 2(b) without the corrugation it takes about 1.8 msec for the local bump ($\delta T_e / \langle T_e \rangle > 0$) to escape the diagnostics view, while in Fig. 2(c) with the corrugation (jet-like $\delta T_e / \langle T_e \rangle$ patterns) it takes about 4 msec. The corrugation impedes the propagation of the avalanche heat flux significantly, acting as transport barriers. These transport barriers will be referred to as the $E \times B$ staircase in this paper with caution that the corresponding measurement of the fine scale radial electric field or the poloidal flow variation is left for future work. The barriers are eventually destroyed and the large avalanche propagates.

On the other hand, Fig. 2(c) is the direct observation of the dynamics between the avalanche and the $E \times B$ staircase, phenomenologically consistent with one idea about their relation, i.e. the jam instability [21]. With the time delay between variations of a field and its flux, the avalanche flux propagation can be jammed to form a seed perturbation (temperature corrugation) for the transport barrier via the feedback [21].

Note that recent gyrokinetic simulations found that there exists such a time delay in both temperature [46] and density [42]. The jamming occurs when the avalanche is so fast to overtake the wave which can be carried by the system. Since the avalanche speed depends on the avalanche heat pulse size in the model [21], it results in the condition that the heat pulse size is larger than some threshold value for the jamming. The relation between the avalanche transport and the staircase will be further discussed later based on analyses of their characteristics (Sections 3 and 4) and the observation of the $E \times B$ staircase formation by the external heat pulse (Section 5).

2.3. The avalanche transport regime in KSTAR

The avalanche transport regime means the particular regime of KSTAR plasmas where ballistic non-diffusive transport events, avalanches, are frequently observed in the absence of the macroscopic MHD instabilities and significant magnetic fluctuations. In terms of operational parameters, this regime corresponds to the toroidal field $B_T = 2.7\text{--}3.0$ T, the plasma current $I_p = 0.5\text{--}0.6$ MA and the edge safety factor $q_{95} = 5.6\text{--}7.0$ with the total ~ 4 MW neutral beam injection (NBI). Plasmas are attached to the inboard limiter to avoid the transition to the high-confinement mode. They have a monotonic q profile. They can have a tearing mode unstable for the low toroidal field which is then suppressed by the additional 1 MW electron cyclotron resonance heating [9].

An example discharge ($B_T = 2.7$ T, $I_p = 0.5$ MA and total 4 MW NBI) in the KSTAR avalanche regime is introduced in Fig. 3. Magnetic fluctuation spectrogram in Fig. 3(a) shows that MHD instabilities such as sawtooth, tearing modes, or edge localized modes are quiescent. The total NBI power was kept constant except short blips for the diagnostics purpose. Time evolutions of typical stability parameters of plasma drift wave instabilities such as magnetic shear $\hat{s} = \frac{r}{q} \frac{dq}{dr}$ and normalized inverse temperature gradient scale lengths $R/L_{T_{i,e}}$ with $L_{T_{i,e}} = \frac{-T_{i,e}}{dT_{i,e}/dr}$ are shown, respectively, in Figs. 3(c), 3(d) and 3(e). Profiles of ion temperature T_i and electron temperature T_e and density n_e at 4.0 sec are shown, respectively, in Figs. 3(f), 3(g) and 3(h). Total (black) and neoclassical (blue) ion and electron heat fluxes are shown in Figs. 3(i) and 3(j), respectively. They are obtained from the power balance analysis using the profiles and TRANSP [47] and NUBEAM [48, 49, 50]. The linear gyrokinetic simulation was performed using the profiles and the global delta f electrostatic gKPSP code with the bounce-averaged kinetic electron and collisions [51, 52]. According to the convention in this work, the negative phase velocity of the linearly most unstable modes means that the ion temperature gradient (ITG) mode may be dominant in this plasma.

The prevalence of the avalanche means that the turbulent transport behavior is non-diffusive, implying that the Kubo number is larger than 1 (see Fig. 6(c)). Unfortunately, it is beyond our capability to accurately and properly estimate τ_{rsd} and τ_{int} to calculate the experimental Kubo number for the relevant turbulence in the KSTAR core plasma.

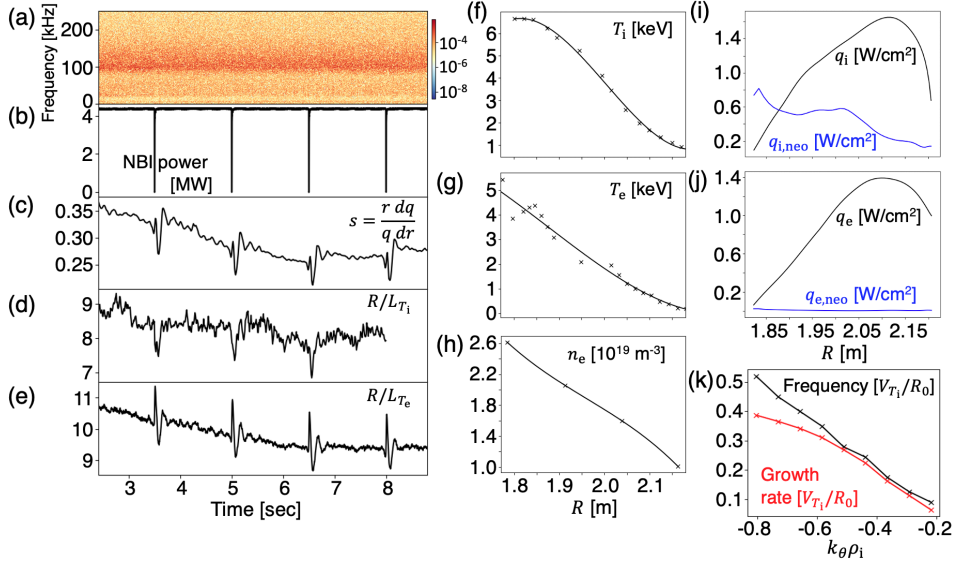


Figure 3. (a) Magnetic fluctuation spectrogram. (b) Total NBI power. (c) Magnetic shear $\hat{s} = \frac{r dq}{q dr}$. (d, e) Normalized inverse temperature gradient scale lengths for ions and electrons $R/L_{T_{i,e}}$ with $L_{T_{i,e}} = \frac{-T_{i,e}}{dT_{i,e}/dr}$, respectively. (f, g, h) Profiles of ion temperature T_i and electron temperature T_e and density n_e at 4.0 sec, respectively. (i, j) Total (black) and neoclassical (blue) ion and electron heat fluxes, respectively. (k) The frequency (black) and the growth rate (red) of the linearly most unstable modes near R_{av} .

2.4. Diagnostics and method

Ion and electron temperature profiles are obtained from the charge exchange recombination spectroscopy [53] and one-dimensional calibrated electron cyclotron emission (ECE) diagnostics [54] in the low field side $R > R_0$, respectively. Density profile is reconstructed from the interferometer with multiple lines of the sight [55].

The one-dimensional ECE diagnostics, the two-dimensional electron temperature fluctuation diagnostics (electron cyclotron emission imaging, ECEI [56]), and the two-dimensional density fluctuation diagnostics (beam emission spectroscopy, BES [57]) are utilized to detect and measure the avalanche. The large avalanche can be identified by finding peaks or valleys in the low-pass filtered T_e time traces. The maximum correlation time lag between T_e data from spatially separated channels is used to measure the propagation speed of the large avalanche. The cross power and cross phase spectra [58] between data from two adjacent channels are used to obtain the spectra of turbulence eddies and the avalanche pseudo-size and to estimate the phase velocity, respectively.

For the detection of the $E \times B$ staircase and the measurement of its characteristics, the high resolution $\delta T_e/\langle T_e \rangle$ data from the ECEI diagnostics [56] in the high field side $R < R_0$ are utilized. Detailed process is explained as follows with two representative cases. Fig. 4(a) shows the T_e trace measured near $R \approx R_{av}$ for some period. A bump of the large avalanche was observed around 3.999 sec. Some of the ECEI channels with good signal-to-noise ratio, indicated by white-filled circles in Fig. 4(d),

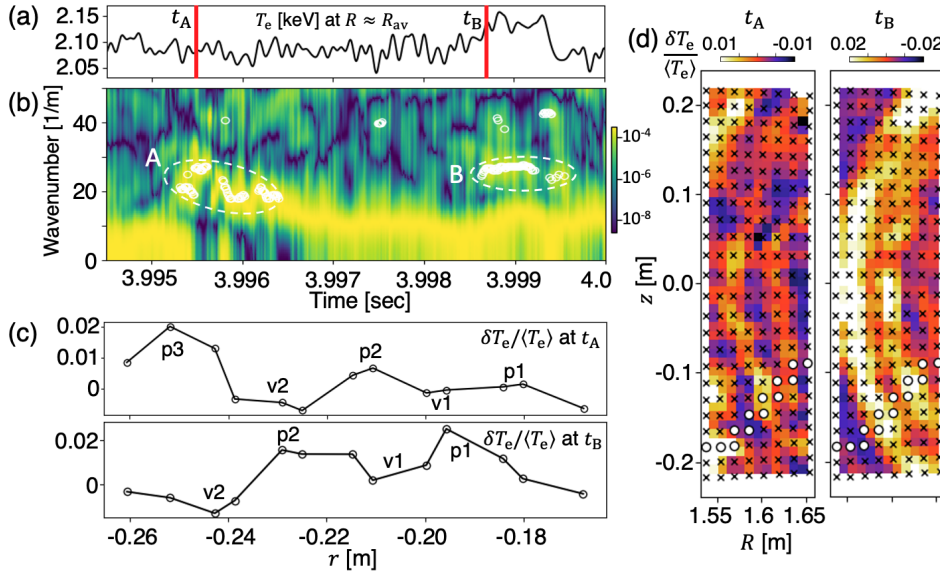


Figure 4. (a) T_e time trace at $R \approx R_{av}$. (b) The radial wavenumber spectrogram obtained using the successive Lomb-Scargle periodograms of the non-uniform radial $\delta T_e / \langle T_e \rangle$ profiles. (c, d) The radial $\delta T_e / \langle T_e \rangle$ profiles and the $\delta T_e / \langle T_e \rangle$ images at times τ_A and τ_B , respectively.

are selected to reconstruct a radial $\delta T_e / \langle T_e \rangle$ profile along the minor radius (r) on the midplane ($z = 0$) as shown in Fig. 4(c). Their measurements on (R, z) space are projected on the midplane following the magnetic flux surface shape of EFIT calculation [59], which provides an enhanced effective radial resolution [60]. The channel position of the ECEI diagnostics was calculated using the forward modelling of the ECE transport [61]. The raw ECEI data was filtered by the boxcar averaging with the averaging window size of $300 \mu\text{s}$ (this boxcar averaging window size is taken as the minimum lifetime for the meaningful detection). Then, the Lomb-Scargle periodogram [62] is used to estimate the radial wavenumber ($k = 1/\Delta$) spectrum for the radially non-uniform $\delta T_e / \langle T_e \rangle$ measurement. The resulting radial wavenumber spectrogram with the successive Lomb-Scargle periodograms is shown in Fig. 4(b). Empty white circles in Fig. 4(b) indicate significant peaks of the radial wavenumber periodogram whose power and also wavenumber are higher than some thresholds. Low radial wavenumber ($k < 18 \text{ m}^{-1}$) peaks are ignored because they are indistinguishable from the trails of the large avalanche in the limited diagnostics view in the experiment. Next, a cluster identification algorithm [63, 64] is used to group close measurements (the temporal separation $< 300 \mu\text{s}$ = the boxcar averaging window size; the radial width (Δ) separation $< 2 \text{ cm}$). Clusters with sufficient lifetime ($\geq 300 \mu\text{s}$) are counted only to avoid possible temporary noise contribution. In Fig. 4(b), the $E \times B$ staircase A and B are found, and A can be classified as the one away from the large avalanche (class A) and B as the other near the large avalanche (class B). This classification is found to be important since they have different Δ distributions, possibly resulting from the avalanche contribution. Radial $\delta T_e / \langle T_e \rangle$ profiles of A and B at times t_A and t_B are shown

in Fig. 4(c), and two-dimensional $\delta T_e / \langle T_e \rangle$ measurements at those times are shown in Fig. 4(d). Values from bad signal-to-noise ratio channels were interpolated in Fig. 4(d). Peaks and valleys of temperature corrugations are indicated by letters ‘p’s and ‘v’s, respectively, and jet-like patterns appear. The staircase B co-exists with the growing bump of the avalanche which corresponds to the low wavenumber component. The lifetime (t_{life}), the power ($|\delta T_e / \langle T_e \rangle|^2$), and the radial tread width (Δ) of the staircase are taken by the temporal width, the average power, and the inverse of the average wavenumber ($\Delta = 1/k$) of the clustered measurements, respectively.

3. Analyses of the avalanche transport

3.1. The ballistic propagation of the avalanche

The analysis of the maximum correlation time lag between the T_e time traces measured by the radial ECE channels shows that the large avalanche heat bump propagates ballistically over the long range. The correlation is calculated using one T_e time trace of the reference channel and the other T_e time trace measured by the channel at the radial distance ΔR . The reference channel is chosen as the one a few centimeter away from the avalanche initiation location R_{av} to minimize the possible interference of the initial avalanche propagation by the $E \times B$ staircase (see Fig. 2(c)). The T_e data are filtered by the low-pass filter to assure that the correlation is determined by the large avalanche heat pulses. The channel distance (ΔR) and the time lag (Δt) have almost a linear relation $\Delta R \sim (\Delta t)^b$ where $b \approx 1$ as shown in Fig. 5(a), meaning the ballistic propagation with the avalanche speed of 60.5 ± 24.5 m/s. The measurement uncertainties in ΔR and Δt represent the estimated uncertainty in the ECE channel position and the standard deviation of multiple measurements. The uncertainty in the avalanche speed is not small because the linearity between ΔR and Δt is not perfect, especially in the edge region. Nonetheless, it is clear that the overall propagation behavior of the avalanche heat pulse is far from diffusive and close to ballistic, and this behavior is consistently observed in the most avalanche plasmas. Note that in the same plasma the approximated mean diamagnetic velocity in the avalanche propagation region is $\overline{\rho_s C_s / a} \approx 720$ m/s where the mean ion sound Larmor radius is $\overline{\rho_s} \approx 1.61 \times 10^{-3}$ m and the mean ion sound speed is $\overline{C_s} \approx 2.02 \times 10^5$ m/s. More complicated behavior [65] is observed in the avalanche plasmas with the continuous electron cyclotron resonance heating, depending on its deposition location against R_{av} . This will be reported in future work with more experiments.

3.2. The parametric dependency of the large avalanche characteristics

The characteristics of the large avalanche such as the propagation speed, the avalanche rate (the number of the avalanche in one second) and the avalanche amplitude (the prominence of the avalanche peak in T_e) are measured, and their parametric dependency is investigated. Measured large avalanche characteristics represent the values of 49–59

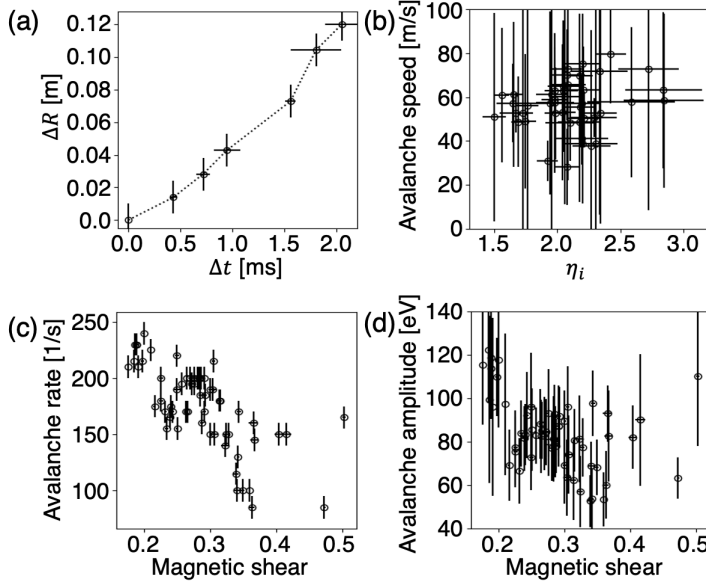


Figure 5. (a) The channel distance ΔR versus the maximum correlation time lag Δt . (b) The average avalanche propagation speed versus $\eta_i \equiv L_n/L_{T_i}$. (c) The avalanche rate versus the magnetic shear. (d) The average avalanche amplitude versus the magnetic shear.

quasi-stationary periods of the multiple KSTAR avalanche plasmas ($B_T = 2.7\text{--}3.0$ T, $I_p = 0.5$ MA, and total 4 MW NBI only). Each quasi-stationary period corresponds to the period of about 0.2 sec. Time averaged values of various physical parameters (the magnetic shear, $R/L_{T_{i,e}}$, R/L_n , the ion collisionality [66], etc) for each period are calculated and compared with the large avalanche characteristics. Note that the physical parameters of the periods differ by the natural plasma evolution (see Fig. 3) and by the different toroidal field.

Among various correlations or anti-correlations (see Fig. 14 in Appendix), some noticeable results are introduced in Figs. 5(b), 5(c) and 5(d). Firstly, the avalanche propagation speed seems to depend on the stability parameter ($\eta_i \equiv L_n/L_{T_i}$) of the ITG mode which is expected to be dominant in this plasma (Section 2.3). Assuming that the linear growth rate of the background turbulence follows $\gamma \sim \eta_i$, the linearity in Fig. 5(b) is consistent with the expected linear dependence of the turbulence front propagation speed on the linear growth rate in the theory [67]. However, measurements are scattered significantly with large uncertainties, and there may be a room for different interpretation. Secondly, as the magnetic shear is decreased, the large avalanche seems to occur more frequently with the larger average amplitude. This might be related to the larger radial size of the ITG turbulence eigenmode with the lower magnetic shear [68, 69], while the linear toroidal mode coupling would be less efficient due to the increased distance between rational surfaces [70, 69].

Although the simple correlation analysis between the plasma parameters and the avalanche and staircase characteristics (Fig. 14) can provide some useful insight, its result should be taken carefully. One reason is that plasma parameters are

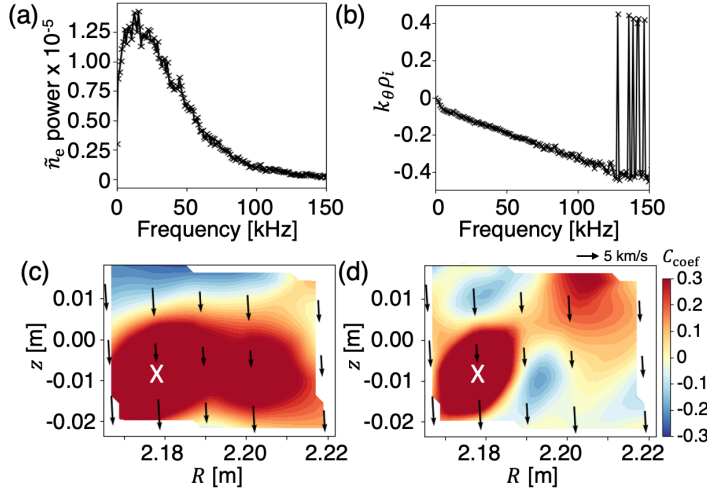


Figure 6. (a) The normalized density fluctuation ($\tilde{n}_e = \delta n_e / \langle n_e \rangle$) power spectrum. (b) The local wavenumber frequency spectrum. The cross correlation coefficient (C_{coef}) images of density fluctuation (50–100 kHz) at the zero time lag in (c) the near-large-avalanche phases and (d) the far-from-large-avalanche phases. The white X indicates the reference channel for the C_{coef} calculation. The length of the black arrows mean the strength of the local laboratory phase velocity $v_{\text{lab}}^{\text{ph}}$.

often strongly correlated with other plasma parameters (the multi-channel transport) in these experiments. The other is that averaged characteristics may not be a meaningful quantity to assess complex phenomena which have long tail distributions of characteristics (see Sections 3.4 and 4.4).

3.3. Edge turbulence eddies with the avalanche

Edge turbulence eddies in the KSTAR avalanche plasma are identified as the ion modes, rotating in the ion diamagnetic drift direction. They are analyzed using the two-dimensional edge density fluctuation measurements from the BES diagnostics [57] in the region of $R = 2.166$ – 2.218 m near the midplane. The density fluctuations from two poloidally adjacent channels are used to calculate the cross power spectrum and the local wavenumber frequency spectrum shown in Figs. 6(a) and 6(b), respectively. The significant fluctuations are detected in the frequency range of 0–120 kHz and the wavenumber range of $-0.4 \leq k_\theta \rho_i \leq 0$. This means a negative (clockwise) poloidal phase velocity in the laboratory frame, i.e. $v_{\text{lab}}^{\text{ph}} = v_{\text{plasma}}^{\text{ph}} + v_{E \times B} = -3.51 \pm 0.41$ km/s. Since the equilibrium $E \times B$ velocity is positive in this plasma, the phase velocity in the plasma frame is expected to be negative along the ion diamagnetic drift direction.

Turbulence eddies form a radially long range coherent structure [71, 72] during the large avalanche. The structure of turbulence eddies is investigated using the cross correlation coefficient (C_{coef}) image between the reference channel (whose location is marked by the white X) and other channels at the zero time lag. The set of the 991 density fluctuation (50–100 kHz) measurements in the near-large-avalanche phases is used for Fig. 6(c), and the set of the 990 measurements in the far-from-large-avalanche

phases (in between the large avalanches) is used for Fig. 6(d). The long range coherent structure of turbulence eddies is observed in Fig. 6(c). Moreover, it is found to appear and disappear quasi periodically with respect to the large avalanche, implying the close relation between this kind of long range structure and the heat flux propagation of the large avalanche [33, 73, 74, 75].

The arrows in Figs. 6(c) and 6(d) indicate the local (near poloidal) $v_{\text{lab}}^{\text{ph}}$ measurements using the cross phase between the 50–100 kHz density fluctuations from poloidally adjacent BES channels. The $v_{\text{lab}}^{\text{ph}}$ measurements in Figs. 6(c) and 6(d) are more or less similar.

3.4. The avalanche pseudo-size distribution

In the KSTAR avalanche plasma, avalanches of various size and scale are observed. Distributions of these quantities would be helpful to infer the physics of the background dynamical process. For example, the avalanche in the system exhibiting the self-organized criticality has power law distributions of the flux size, the spatial scale and the temporal scale [76]. The criticality means that there is no characteristic scale based on local physics and the pdf obeys the power law distribution, exhibiting the self-similarity.

However, the measurement of the flux size and the scales for all avalanches is challenging. The accurate heat flux size would require the high resolution simultaneous measurement of density and temperature variations associated with the avalanche. Also, the spatial scale of the small avalanches can be significantly affected by the finite diffusive transport. In JT-60U, the average electron heat flux by the avalanche was estimated using the measured temperature variation (neglecting the small density variation). It reveals that the average avalanche heat flux accounts for the significant fraction of the heat flux increase as the heating power increases [38], but the distribution of the heat flux was not provided. In previous analysis of the KSTAR avalanche [9], instead of the distribution of the avalanche temporal scale, the power law correlation function (the power law frequency spectrum) and the large Hurst exponent $H > 0.5$ were provided, suggesting the long temporal correlation or the temporal criticality [3].

On the other hand, the frequency spectrum of $|\delta T_e/\langle T_e \rangle|^2$ may be thought as the pseudo-size distribution of the avalanche. The pseudo-size is defined as the volume of the temperature perturbation by one avalanche, i.e. height \times width \times length $= \delta T_e \times \delta R \times 2\pi R \sim \delta T_e^2$ where δR is the radial width of the avalanche heat pulse and it is assumed to linearly depend on δT_e . The cross power ($|\delta T_e/\langle T_e \rangle|^2$) spectrum obtained using two poloidally adjacent ECEI channels near R_{av} is shown in Fig. 7(a). The local wavenumber frequency spectrum in Fig. 7(b) shows that the measured coherent temperature fluctuations indeed correspond to $m = 0$ temperature variations by transport events rather than turbulence eddies. The power spectrum follows the power law $S(f) \propto f^{-0.7}$, meaning the power law distribution of the avalanche pseudo-size.

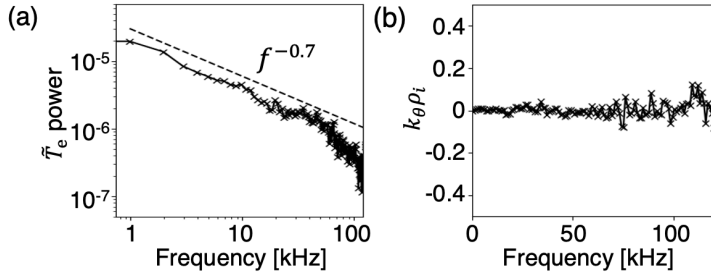


Figure 7. (a) The normalized electron temperature fluctuation power spectrum. (b) The local wavenumber frequency spectrum.

4. Analyses of the $E \times B$ staircase

4.1. The initial formation and transformation of the $E \times B$ staircase

The initial formation and their transformations have been revealed by investigating the long range vertical $\delta T_e / \langle T_e \rangle$ profiles obtained in the previous experiment [9]. Fig. 8(a) shows the formation process of the $E \times B$ staircase introduced in Figs. 1(b) and 1(c). Initially, a localized perturbation near R_{av} arises. The perturbation grows in size, propagates toward the plasma center with the speed of 100 m/s which is anomalously fast [77], and results in the globally self-organized mini barriers with the meso-scale vertical tread width $\Delta_z = 10.8$ cm. They dissipate in time with appearance of an $m = 1$ structure for about 1 msec, but reform repeatedly [9]. In addition, both increase and decrease of the $E \times B$ staircase width are observed as shown in Figs. 8(b) and 8(c). In Fig. 8(b) the weak amplitude and small width staircase ($\Delta_z \approx 10$ cm) grows to have the stronger amplitude and larger width ($\Delta_z \approx 20$ cm). It is worth noting that merging of small scale transport barriers [78] has been considered one possible way to form a large scale strong transport barrier [23]. In addition, a sudden merger or disappearance of multiple zonal-band structures leading to a few broader zonal jets has been observed in long term simulation of forced two-dimensional barotropic incompressible flows in the geofluid dynamics context [79]. Although the resulting larger barriers in Fig. 8(b) dissipate in time possibly through the collisional damping (see Fig. 10(a)), the increased δT_e amplitude implies the stronger transport regulation for the larger width staircase. In Fig. 8(c) the opposite transformation is shown. The initial $\Delta_z \approx 25$ cm staircase becomes about the half width within 0.3 msec. Observations in KSTAR plasmas show that the $E \times B$ staircase is persistent but not stationary (destruction, reformation and transformation), which is consistent with the observations in the gyrokinetic simulations [12, 7].

4.2. Edge turbulence eddies with the $E \times B$ staircase

The structure of edge turbulence eddies during the $E \times B$ staircase phases is radially more limited, compared to that during the near-large-avalanche phases in Fig. 6(c). In Fig. 9(a), the cross correlation coefficient (C_{coef}) image at the zero time lag is shown.

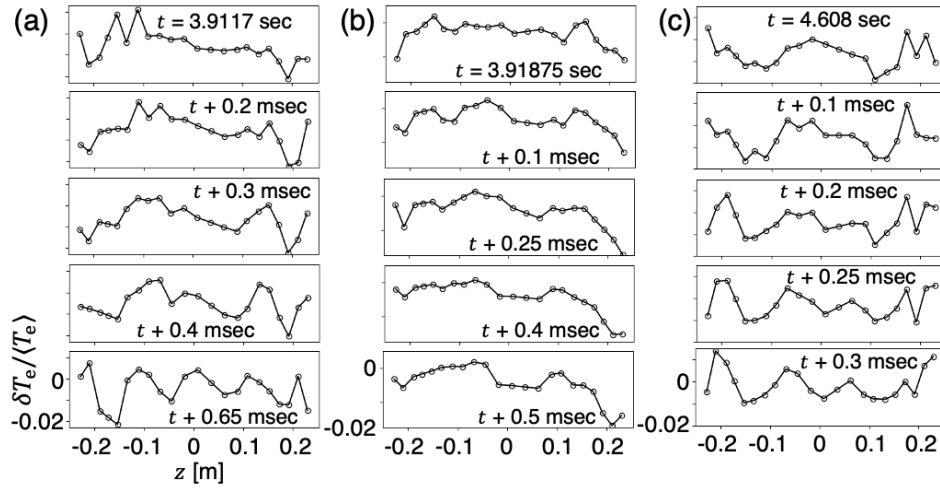


Figure 8. (a) The initial formation of the $E \times B$ staircase (class A). (b) Transformation of the smaller scale ($\Delta_z \approx 10$ cm) staircase to the larger scale ($\Delta_z \approx 20$ cm) staircase. (c) Transformation of the larger scale ($\Delta_z \approx 25$ cm) staircase to the smaller scale ($\Delta_z \approx 12$ cm) staircase.

It is obtained using the set of the 102 density fluctuation (50–100 kHz) measurements in the staircase phases during which the staircase of the radial tread width $\Delta = 2$ –3 cm exists. It seems that the radial extent of the strongly correlated region is limited by the tread width of the $E \times B$ staircase, i.e. the distance between the shear flow layers.

The analysis of the auto-bicoherence in density fluctuations suggests that the zonal density (\sim potential) field, constituting the $E \times B$ shear flow layer, is enhanced near the edge of the correlated structure through the nonlinear energy transfer from turbulence. Fig. 9(b) shows the two-dimensional plot of the average local bicoherence with $f_3 \approx 0$. The bicoherence measures the degree of the three-wave coupling among fluctuations of frequencies f_1 , f_2 , and $f_3 = f_1 + f_2$ [58]. The local density fluctuation measured by each BES channel is used to calculate the local squared auto-bicoherence (b^2) as shown in Fig. 9(c). The b^2 is averaged over the fluctuations pairs with $f_3 \approx 0$ (along the $f_2 = -f_1$ line) to give $\sum_{f_1, f_2} b^2(f_3 \approx 0)/N$ where N is the number of fluctuation pairs with $f_3 \approx 0$. The relatively large $\sum_{f_1, f_2} b^2(f_3 \approx 0)/N$ is observed near both edges ($R = 2.167$ m and $R = 2.19$ m) of the correlated structure, implying that the developed zonal flow shear there interferes the long range coupling of turbulence eddies.

The local $v_{\text{lab}}^{\text{ph}}$ measurements in the staircase phases, indicated by the black arrows in Fig. 9(a), show the significant variation around the large $\sum_{f_1, f_2} b^2(f_3 = 0)/N$ regions, compared to the $v_{\text{lab}}^{\text{ph}}$ measurements in the near-large-avalanche phases in Fig. 6(c). It seems that the length of the arrow (the strength of the $v_{\text{lab}}^{\text{ph}}$) increases on the right side of the large $\sum_{f_1, f_2} b^2(f_3 = 0)/N$ region (for example, at $R = 2.167$ m and $z = -0.015$ m) and decreases on the left side (for example, at $R = 2.178$ m and $z = -0.015$ m). This implies the positive zonal potential perturbation in the large $\sum_{f_1, f_2} b^2(f_3 \approx 0)/N$ region.

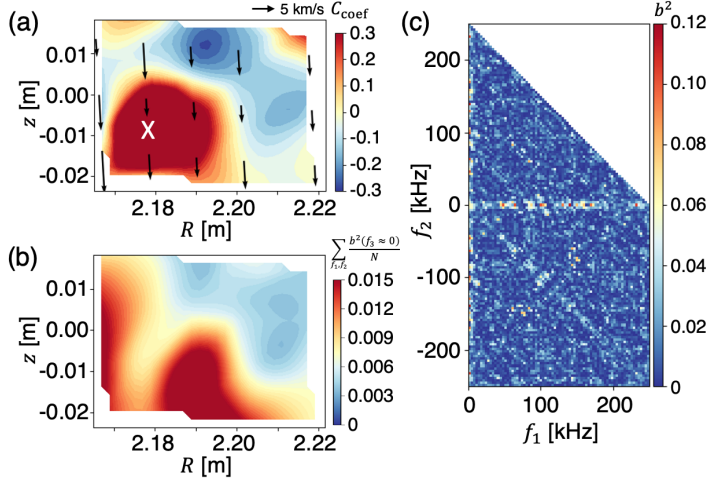


Figure 9. (a) The cross correlation coefficient (C_{coef}) images of density fluctuation (50–100 kHz) at the zero time lag with the $E \times B$ staircase. The white X indicates the reference channel for the C_{coef} calculation. The length of the black arrows mean the strength of the local laboratory phase velocity $v_{\text{lab}}^{\text{ph}}$. (b) The average bicoherence image with $f_3 \approx 0$ kHz. (c) The bicoherence of density fluctuations at $R = 2.19$ m and $z = -0.02$ m.

4.3. The parametric dependency of the $E \times B$ staircase

The characteristics of the $E \times B$ staircase such as the staircase ratio, the lifetime, the power and the radial tread width are measured, and their parametric dependency is investigated. The Lomb-Scargle periodograms [62] of non-uniform $\delta T_e / \langle T_e \rangle$ measurements and the cluster algorithm [63, 64] are used to identify the staircase and extract its characteristics (see Section 2.4). The measurements for the quasi-stationary periods mentioned in Section 3.2 are used, and the same caution would apply.

The most noticeable relation is found between the staircase ratio and the ion collisionality [66] as shown in Fig. 10(a). The staircase ratio is defined as the staircase-detected-fraction of each analysis period. The overall anti-correlation between the staircase ratio and the collisionality means that the staircase is observed for the relatively shorter time in the higher collisionality regime. The average lifetime and the collisionality in Fig. 10(b) have shown the more scattered anti-correlation. Note that the lifetime distribution seems to have a long tail (see Section 4.4).

4.4. Distributions of the $E \times B$ staircase characteristics

Numerous measurements of the $E \times B$ staircase were obtained for the similar 23 quasi-stationary periods from 4 repeated discharges to investigate the distributions of its characteristics. These similar quasi-stationary periods are characterized by the magnetic shear $\hat{s} = \frac{r}{q} \frac{dq}{dr} = 0.23\text{--}0.35$, the normalized ion and electron temperature gradients $R/L_{T_i} = 7.5\text{--}9$ and $R/L_{T_e} = 9.0\text{--}10.5$, the ion collisionality [66] = 0.18–0.215 and plasma stored energy = 300–320 kJ.

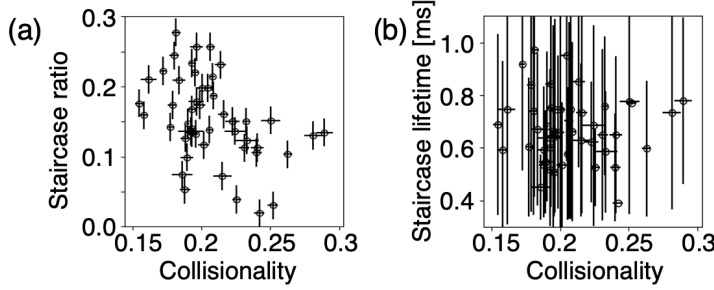


Figure 10. (a) The $E \times B$ staircase ratio versus the ion collisionality. (b) The average $E \times B$ staircase lifetime versus the ion collisionality.

As explained in Section 2.4, the $E \times B$ staircase are classified in two classes A (away from the large avalanche) and B (near the large avalanche). This classification is found to be important since they have shown different width distributions (see below). Total 123 staircases are found for the class A and 659 staircases for the class B. The lifetime (t_{life}), the power ($|\delta T_e/\langle T_e \rangle|^2$) and the radial tread width (Δ) probability distributions of the class A barriers are shown in Figs. 11(a), 11(c), and 11(e), and those of the class B are shown in Figs. 11(b), 11(d) and 11(f), respectively.

Distributions of the lifetime and power do not differ much between the class A and the class B. For example, the lifetime distributions of both classes can be fitted with a power-law (t_{life}^{-a}) function with a coefficient a changing around 1 msec as shown in Figs. 11(a) and 11(b). The power-law distribution of the lifetime implies non-existence of the characteristic lifetime and the critical behavior in time. However, the range of the lifetime may be too narrow to conclude, and an exponential distribution ($e^{-at_{\text{life}}}$) with a characteristics time ($1/a$) also provided a fair agreement. The power probability distributions of both classes have shown a positive skewness $S > 0$ and a kurtosis $K > 3.0$ as shown in Figs. 11(c) and 11(d). The non-Gaussianity of distributions means that the large power staircase is rare but observed.

Unlike other distributions, the radial tread width (Δ) probability distributions of the class A and the class B look different. While the distribution of the class A seems more or less random, the distribution of the class B has a positive skewness fat tail for $\Delta \geq 2.7$ cm with an independent peak around $\Delta \approx 2.5$ cm. It is found that the fat tail of the Δ distribution of the class B shows the reasonable agreement with the constant multiple of a Frechet distribution $F(\Delta) = \frac{\tau^{1+\kappa}}{\sigma} e^{-\tau}$ with $\tau = (1 + \kappa \frac{\Delta - \Delta_\mu}{\sigma})^{-1/\kappa}$, where the shaping parameter $\kappa = 0.80$, the location parameter $\Delta_\mu = 3.81$ cm and the scale parameter $\sigma = 1.14$. The parameters are obtained by the least-square fit. By the Anderson-Darling test [80, 81], the null hypothesis that the class B width samples follow the Frechet distribution with the given parameters may not be rejected since the p-value is found to be higher than 25 % (the test is capped at 25 %). This is qualitatively consistent with the gyrokinetic simulation result [7], where the width measurements were obtained over a broad range of normalized gyro-radius, and their distribution follows a Frechet distribution with the different parameters [82]. The distinguished Frechet

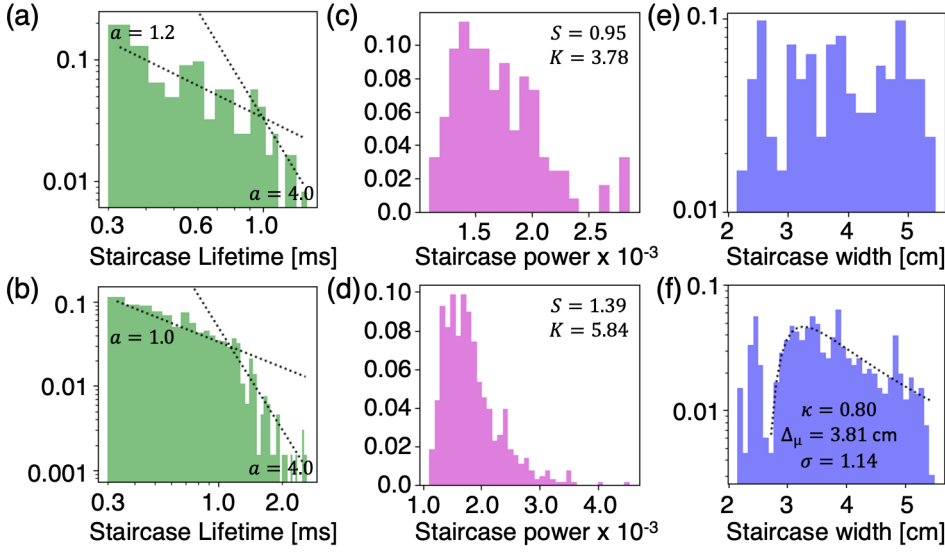


Figure 11. Normalized probability distributions of the lifetime, the power, and the radial tread width of the $E \times B$ staircase (a, c, e; top) away from the large avalanche (class A) and (b, d, f; bottom) near the large avalanche (class B), respectively. Dotted lines indicate constant multiples of power-law t_{life}^{-a} for the lifetime distribution and a Frechet distribution with the shaping (κ), location (Δ_μ) and scale (σ) parameters for the width distribution.

distribution for the $E \times B$ staircase close to the large avalanche might result from the influence of large avalanche on the staircase formation as discussed in the following Section 5.

5. Conclusion and discussion

The $E \times B$ staircase, globally self-organized mini transport barriers, is observed in the KSTAR avalanche transport regime [9]. The detail experimental approach and methods for the detection and analyses are explained in Section 2. Since the characteristics of underlying transport is closely associated with the mechanism and characteristics of the self-organization phenomena in the non-equilibrium complex system, various aspects of both the avalanche transport (Section 3) and the $E \times B$ staircase (Section 4) have been analyzed and presented in this work. Before discussing how these analyses can lead to the improved understanding of their physical relation, the main findings of the analyses are summarized as follows.

For the avalanche,

- (i) The heat bump propagation of the large avalanche shows a non-diffusive ballistic behavior (Section 3.1).
- (ii) The average propagation speed of the large avalanche heat bump ranges over 20–80 m/s in different quasi-stationary periods, showing a scattered correlation with η_i . The large avalanche is more frequently observed with the stronger amplitude in the weaker magnetic shear period (Section 3.2).

- (iii) Edge turbulence eddies of the ion modes form a radially coupled long range structure during the large avalanche phase (Section 3.3).
- (iv) The pseudo-size distribution of the avalanche follows the power law distribution (Section 3.4).

For the $E \times B$ staircase,

- (i) It is classified into the one that forms away from the large avalanche (class A) and the other near the large avalanche (class B) (Section 2.4). The number of the class A staircase observation (123) is smaller than the number of the class B staircase observation (659) for the same periods, meaning that the staircase favors to be found around the large avalanche.
- (ii) The formation process of both classes (Fig. 8(a) for the class A and Fig. 2(c) for the class B) shows that the staircase starts to form with some initial heat (and probably momentum) perturbation.
- (iii) The radial tread width of the staircase changes in time (Section 4.1). The staircase is persistent but not stationary.
- (iv) Edge turbulence eddies show a radially more limited structure during the staircase phase with the zonal density (\sim potential) component. The significant three-wave coupling between the zonal component and turbulence is observed only for the staircase phase not for the large avalanche phase, which is concomitant with the larger spatial variation of $v_{\text{lab}}^{\text{ph}}$ in the former (Section 4.2).
- (v) The staircase is observed for the longer time in the lower collisionality period (Section 4.3).
- (vi) Distributions of the lifetime, the power and the radial tread width of the staircase are obtained for the similar quasi-stationary periods. The distinguished width distribution of the class B staircase can be well fit by a Frechet distribution (Section 4.4).

To begin the discussion, the higher likelihood of finding the $E \times B$ staircase near the large avalanche suggests that the staircase requires an initial heat and/or momentum perturbation larger than some threshold value. This naturally relates the avalanche transport with the staircase and also provides the explanation of the Frechet-like width distribution for the staircase near the large avalanche. The required perturbation for the staircase can be provided by the large avalanche. The power-law distribution of the avalanche pseudo-size $P(S) \sim S^{-\alpha}$ means that the large event, which can satisfy the threshold, is rare but occurs. The size of the heat perturbation may not be the sufficient condition, because there is the large avalanche having the comparable heat perturbation but not followed by the staircase formation (Fig. 2(b)). As pointed out in the gyrokinetic simulation [15], the radial synchronization and the synergetic effect between the mean E_r field variation by the large avalanche and the turbulence zonal field can be important. On the other hand, the Frechet distribution can follow if it is assumed that the staircase width (Δ) depends on the pseudo-size ($S \equiv \delta T_e^2 \sim \delta T_e \delta R$)

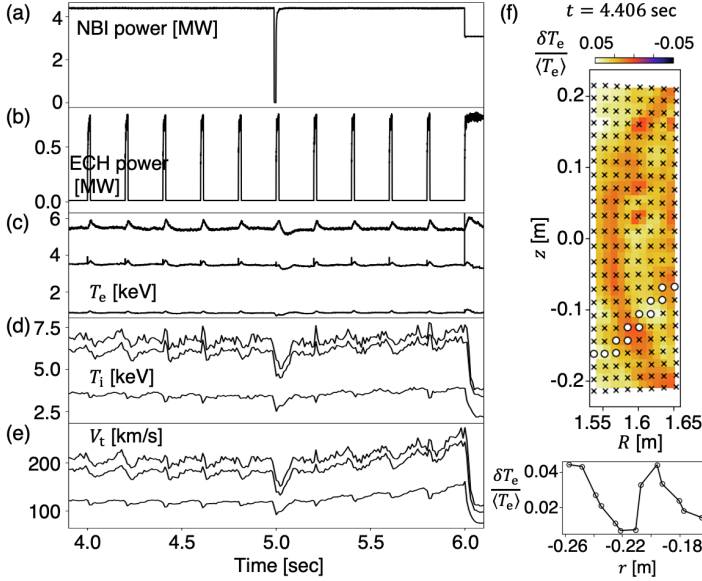


Figure 12. (a) Total NBI power. (b) ECH power. (c, d, e) Electron temperature, ion temperature and ion toroidal velocity measured at different radial locations, respectively. (f) The radial $\delta T_e / \langle T_e \rangle$ profile and the $\delta T_e / \langle T_e \rangle$ images at 4.406 sec.

of the associated large avalanche. The Frechet distribution is one of the extreme value distributions, corresponding to a distribution of maxima of samples when samples follow a distribution of the long tail such as the power law function [83]. Since the avalanche pseudo-size follows the power law distribution $P(S) \sim S^{-\alpha}$ and the staircase threshold can be satisfied with the rare and large avalanche (the maximum of each long period, $\max \{S\}$), the staircase width distribution $P(\Delta \sim \max\{S\})$ would follow the Frechet distribution.

For validation of the staircase threshold, perturbation and response experiments with carefully controlled perturbations would be required. Although the fine scan of the perturbation size was not possible, the constant external heat perturbation could be applied using the modulated electron cyclotron resonance heating (MECH) to investigate the response of the KSTAR avalanche plasma as shown in Fig. 12. The short pulses of the MECH induced the rapid and significant perturbation on the electron and ion temperature as well as the ion momentum in the almost entire radial region. The size of the MECH perturbation on the electron temperature was almost twice that of the large avalanche observed around. Interestingly, the $E \times B$ staircase of the relatively large width $\Delta \geq 6$ cm is partly observed a few millisecond after the every MECH heat pulse injection. The one example observation at 4.406 sec is shown in Fig. 12(f). This suggests that the assumption made in previous discussion, i.e. the staircase width depends on the associated perturbation size, can be valid, though more quantitative experiment and analysis are necessary. Note that the jam instability model of the staircase [21], introduced briefly in Section 2.2, suggested the threshold condition on the heat pulse size, originated from the dependency of the avalanche propagation

DP in $x+t$	Wet site	Dry site	Death	Offspring	Coalescence	Diffuse left	Diffuse right	$p < p_c$	$p > p_c$
	●	○	○○	●●	●●	●○	○●	Fully dry sites ○○○○○○	Active phase with infinite $\xi_{\perp\parallel}$
Staircase dynamics in $k+t$	Mode ~~~~~	Damped mode ~~~~~	~~~~~ ~~~~~	~~~~~ ~~~~~	~~~~~ ~~~~~	~~~~~	~~~~~	Fully damped modes	Infinite ξ_{\parallel} (lifetime ^a) Infinite ξ_{\perp} : infinite $k_s \rightarrow \delta(x)$ (one large barrier)

Figure 13. Analogy between the directed percolation (DP) in the space-time ($x+t$) space and the staircase dynamics in the wavenumber-time ($k+t$) space. Diffusion (Figs. 8(b) and 8(c)), offspring and coalescence of the staircase in the $k+t$ space were observed in the experiment.

speed on the heat pulse size. The propagation speed of the MECH perturbation is found to be also relatively higher ~ 100 m/s, compared to the heat bump propagation speed of the large avalanche (< 75 m/s) in the same plasma.

Secondly, both the avalanche transport and the $E \times B$ staircase exhibit the critical features that their initial localized perturbation can propagate rapidly over the whole system and generate structures of the macroscopic correlation length (Figs. 5(a), 6(c) and 8(a)). The central task would be to understand how their critical features manifest and how they are related to the other non-equilibrium critical phenomena. The critical features of the avalanche heat transport in tokamak plasmas have been relatively better understood in association with the self-organized criticality (SOC) [29]. The avalanche in the SOC system operates by the domino effect over the near marginal profile, i.e. the successive destabilization of nearby locations by the flux propagation [2, 3]. However, how the localized momentum perturbation propagates the long range and the correlated structure of zonal flows, the $E \times B$ staircase, appears are less understood. The inter-shear-layer avalanches might mediate their interactions by delivering the Reynolds stress momentum [82] (Fig. 9(b)). The power-law-like distribution of the staircase lifetime (Figs. 11(a) and 11(b)) and the fast propagation of the initial perturbation (Fig. 8(a)) might imply another kind of avalanche composed of the momentum flux propagation [84, 85] in the SOC system. Or, the phase space structure might play a role [40, 41].

Nonetheless, considering the $E \times B$ staircase as the self-organization near an non-equilibrium critical state can provide a new perspective to understand its characteristics and evolution by an analogy with a directed percolation (DP) (see Fig. 13). The directed percolation is one of the most studied non-equilibrium critical phenomena [1]. Its typical configuration is the two-dimensional tilted lattice where each site is either wet or dry and connected by bonds. Each bond can be active with the probability p , and the wet site can propagate in a given direction through the active bond. The parallel axis to the propagation is taken as the time (t) axis, and the spatio-temporal evolution of the system can be studied as p varies. If p is smaller than some critical value p_c , the system ends up with a fully dry absorbing state with finite correlation lengths. If $p \geq p_c$, the system falls into an active state with infinitely percolating wet sites. The non-stationary and persistent dynamics of the staircase in the wavenumber-time ($k+t$) space (Fig. 4(b))

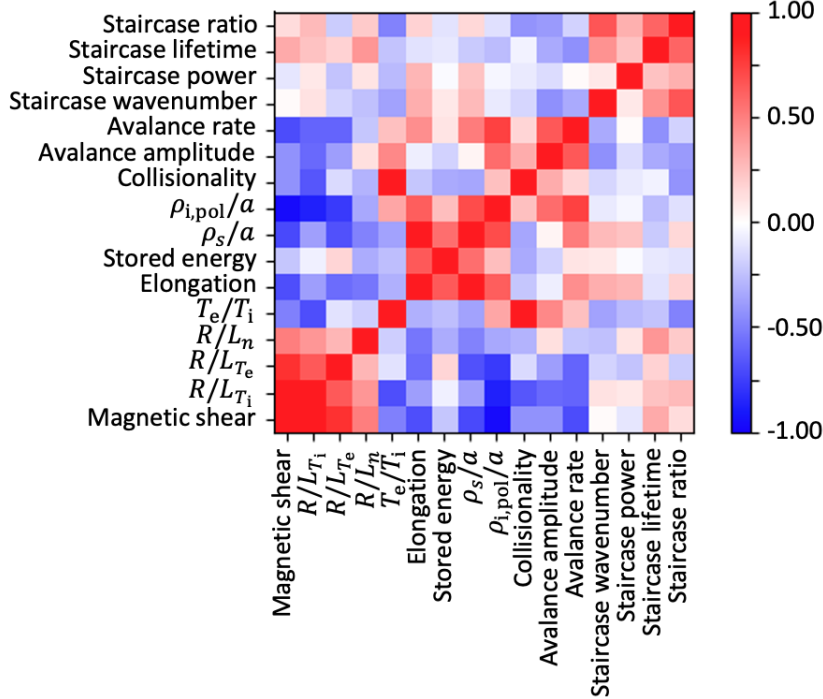


Figure 14. The colormap represents the correlation coefficients among various plasmas parameters and characteristics of the large avalanche and the $E \times B$ staircase.

can be thought as a DP process with slow drive and many absorbing states. Then, near the active state, the infinitely percolating modes (ks) in the staircase $k + t$ space would correspond to the one large long standing transport barrier, i.e. the stationary internal transport barrier [86]. The power-law-like distribution of the lifetime is not inconsistent with this view of the staircase.

Finally, two important future works will be mentioned briefly. In this work, most analyses are limited to the electron heat transport due to the lack of the high resolution ion temperature and velocity diagnostics. Significant variations of the ion temperature and velocity by the largest avalanche in the KSTAR plasma were identified, but the insufficient spatio-temporal resolution of the diagnostics prevents the meaningful analysis. Analyses of the ion temperature avalanche and corrugation with the improved diagnostics would be valuable. Also, the size scaling study of the $E \times B$ staircase characteristics using the inter-machine data would be desirable.

Appendix

Acknowledgments

One of the authors (M.J.C.) acknowledges helpful discussions with K. Razumova, Y. Kishimoto, Y. Kosuga, W. Wang, K. Ida, T. Kobayashi, F. Kin and M. Sasaki during the UNIST-Kyoto University workshop, the Asia-Pacific Transport Working Group meeting, the Asia-Pacific Conference on Plasma Physics and elsewhere. This work was supported

by R&D Programs of “KSTAR Experimental Collaboration and Fusion Plasma Research (EN2301-14)” and “High Performance Fusion Simulation R&D (EN2341-9)” through Korea Institute of Fusion Energy (KFE) funded by the Government funds. Computing resources were provided on the KFE computer, KAIROS, funded by the Ministry of Science and ICT of the Republic of Korea (EN2341-9).

Competing interests

The authors declare no competing interests.

Data availability

Data are available from the corresponding author upon request.

References

- [1] Livi R and Politi P 2017 *Nonequilibrium statistical physics* (Cambridge University Press) ISBN 978-1-107-04954-3
- [2] Hahm T S and Diamond P H 2018 *Journal of the Korean Physical Society* **73** 747
- [3] Sanchez R and Newman D E 2015 *Plasma Physics and Controlled Fusion* **57** 123002
- [4] Nicolis G and Prigogine I 1989 *Exploring complexity* (W. H. Freeman and Company) ISBN 0-7167-1859-6
- [5] Goldenfeld N and Kadanoff L P 1999 *Science* **284** 87 ISSN 0036-8075
- [6] Dif-Pradalier G, Diamond P H, Grandgirard V, Sarazin Y, Abiteboul J, Garbet X, Ghendrih P, Strugarek A, Ku S and Chang C S 2010 *Physical Review E* **82** 025401(R)
- [7] Dif-Pradalier G, Hornung G, Garbet X, Ghendrih P, Grandgirard V, Latu G and Sarazin Y 2017 *Nuclear Fusion* **57** 066026
- [8] Diamond P H, Itoh S I, Itoh K and Hahm T S 2005 *Plasma Physics and Controlled Fusion* **47** R35
- [9] Choi M J, Jhang H, Kwon J M, Chung J, Woo M, Qi L, Ko S, Hahm T S, Park H K, Kim H S, Kang J, Lee J, Kim M, Yun G S and Team t K 2019 *Nuclear Fusion* **59** 086027
- [10] Ashourvan A, Nazikian R, Belli E, Candy J, Eldon D, Grierson B A, Guttenfelder W, Haskey S R, Lasnier C, McKee G R and Petty C C 2019 *Physical Review Letters* **123** 115001
- [11] Liu W, Chen Y, Ke R, McKee G, Yan Z, Fang K, Yang Z, Gao Z, Tan Y and Tynan G R 2021 *Physics of Plasmas* **28** 012512 ISSN 1070-664X
- [12] Ghendrih P, Norscini C, Cartier-Michaud T, Dif-Pradalier G, Abiteboul J, Dong Y, Garbet X, Gürcan O, Hennequin P, Grandgirard V, Latu G, Morel P, Sarazin Y, Storelli A and Vermare L 2014 *The European Physical Journal D* **68** 303 ISSN 1434
- [13] Villard L, McMillan B F, Sauter O, Hariri F, Dominski J, Merlo G, Brunner S and Tran T M 2014 *Journal of Physics: Conference Series* **561** 012022
- [14] Dominski J, Brunner S, Görler T, Jenko F, Told D and Villard L 2015 *Physics of Plasmas* **22** 062303
- [15] Wang W, Kishimoto Y, Imadera K, Li J Q and Wang Z X 2018 *Nuclear Fusion* **58** 056005
- [16] Qi L, Kwon J M, Hahm T S, Yi S and Choi M J 2019 *Nuclear Fusion* **59** 026013
- [17] Rath F, Peeters A G and Weikl A 2021 *Physics of Plasmas* **28** 072305 ISSN 1070-664X
- [18] Dif-Pradalier G, Hornung G, Ghendrih P, Sarazin Y, Clairet F, Vermare L, Diamond P H, Abiteboul J, Cartier-Michaud T, Ehrlacher C, Esteve D, Garbet X, Grandgirard V, Gurcan O D, Hennequin P, Kosuga Y, Latu G, Maget P, Morel P, Norscini C, Sabot R and Storelli A 2015 *Physical Review Letters* **114** 085004

- [19] Hornung G, Dif-Pradalier G, Clairet F, Sarazin Y, Sabot R, Hennequin P and Verdoolaege G 2017 *Nuclear Fusion* **57** 014006
- [20] van Milligen B, Carreras B, García L and Nicolau J 2019 *Entropy* **21** 148
- [21] Kosuga Y, Diamond P H and Gurcan O D 2013 *Physical Review Letters* **110** 105002
- [22] Itoh K and Itoh S I 2016 *Plasma Physics and Controlled Fusion* **58** 045017 ISSN 0741-3335
- [23] Ashourvan A and Diamond P H 2016 *Physical Review E* **94** 051202(R)
- [24] Guo W, Diamond P H, Hughes D W, Wang L and Ashourvan A 2019 *Plasma Physics and Controlled Fusion* **61** 105002
- [25] Sasaki M, Itoh K, McMillan B F, Kobayashi T, Arakawa H and Chowdhury J 2021 *Physics of Plasmas* **28** 112304 ISSN 1070-664X
- [26] Garbet X, Panico O, Varennes R, Gillot C, Dif-Pradalier G, Sarazin Y, Grandgirard V, Ghendrih P and Vermare L 2021 *Physics of Plasmas* **28** 042302 ISSN 1070-664X
- [27] Leconte M and Kobayashi T 2021 *Physics of Plasmas* **28** 014503
- [28] Yan Q and Diamond P H 2022 *Nuclear Fusion* **62** 126032 ISSN 0029-5515
- [29] Diamond P H and Hahm T S 1995 *Physics of Plasmas* **2** 3640
- [30] Carreras B A, Newman D, Lynch V E and Diamond P H 1996 *Physics of Plasmas* **3** 2903
- [31] Idomura Y, Urano H, Aiba N and Tokuda S 2009 *Nuclear Fusion* **49** 065029
- [32] Ku S, Chang C S and Diamond P H 2009 *Nuclear Fusion* **49** 115021
- [33] Sarazin Y, Grandgirard V, Abiteboul J, Allfrey S, Garbet X, Ghendrih P, Latu G, Strugarek A and Dif-Pradalier G 2010 *Nuclear Fusion* **50** 054004
- [34] Politzer P A 2000 *Physical Review Letters* **84** 1192
- [35] Pan O, Xu Y, Hidalgo C, Zhong W L, Shi Z B, Ji X Q, Jiang M, Feng B B, Zhou Y, Cheng J, Liu Y, Xu M, Chen W, Ding X T, Yan L W, Yang Q W, Duan X R and Liu Y 2015 *Nuclear Fusion* **55** 113010
- [36] Van Compernolle B and Morales G J 2017 *Physics of Plasmas* **24** 112302
- [37] Zhang B, Inagaki S, Hasamada K, Yamasaki K, Kin F, Nagashima Y, Yamada T and Fujisawa A 2019 *Plasma Physics and Controlled Fusion* **61** 115010
- [38] Kin F, Itoh K, Bando T, Shinohara K, Oyama N, Yoshida M, Kamiya K and Sumida S 2023 *Nuclear Fusion* **63** 016015 ISSN 0029-5515
- [39] Gillot C, Dif-Pradalier G, Sarazin Y, Bourdelle C, Navarro A B, Camenen Y, Citrin J, Sieni A D, Garbet X, Ghendrih P, Grandgirard V, Manas P and Widmer F 2023 *Plasma Physics and Controlled Fusion* **65** 055012 ISSN 0741-3335 (Preprint [2209.04064](https://arxiv.org/abs/2209.04064))
- [40] Diamond P H, Itoh S I and Itoh K 2010 *Modern plasma physics* (Cambridge University Press)
- [41] Kosuga Y and Diamond P H 2011 *Physics of Plasmas* **18** 122305 ISSN 1070-664X
- [42] Qi L, Choi M, Leconte M, Hahm T and Kwon J M 2022 *Nuclear Fusion* **62** 126025
- [43] van Milligen B P, Carreras B A, Hidalgo C, Cappa A and Team T I 2018 *Physics of Plasmas* **25** 062503
- [44] Milligen B P v, Hoefel U, Nicolau J H, Hirsch M, García L, Carreras B A, Hidalgo C and Team T W X 2018 *Nuclear Fusion* **58** 076002
- [45] Park H K, Choi M J, Hong S H, In Y, Jeon Y M, Ko J S, Ko W H, Kwak J G, Kwon J M, Lee J, Lee J H, Lee W, Nam Y B, Oh Y K, Park B H, Park J K, Park Y S, Wang S J, Yoo M, Yoon S W, Bak J G, Chang C S, Choe W H, Chu Y, Chung J, Eidietis N, Han H S, Hahn S H, Jhang H G, Juhn J W, Kim J H, Kim K, Loarte A, Lee H H, Lee K C, Mueller D, Na Y S, Nam Y U, Park G Y, Park K R, Pitts R A, Sabbagh S A, Yun G S and team t K 2019 *Nuclear Fusion* **59** 112020
- [46] Muto M, Imadera K and Kishimoto Y 2021 *Physics of Plasmas* **28** 082304 ISSN 1070-664X
- [47] Breslau J, Gorelenkova M, Poli F, Sachdev J, Pankin A, Perumpilly G, Yuan X, Glant L and of Science U O 2018 Transp URL <https://www.osti.gov/biblio/1489900>
- [48] Hawryluk R J *et al.* 1980 An empirical approach to tokamak transport physics of plasmas close to thermonuclear conditions *Brussels: CEC*
- [49] Goldston R, McCune D, Towner H, Davis S, Hawryluk R and Schmidt G 1981 *Journal of*

Computational Physics **43** 61 ISSN 0021-9991

- [50] Pankin A, McCune D, Andre R, Bateman G and Kritz A 2004 *Computer Physics Communications* **159** 157 ISSN 0010-4655
- [51] Qi L, Kwon J, Hahm T S and Jo G 2016 *Physics of Plasmas* **23** 062513
- [52] Kwon J M, Qi L, Yi S and Hahm T 2017 *Computer Physics Communications* **215** 81 ISSN 0010-4655
- [53] Ko W H, Oh S and Kwon M 2010 *IEEE Transactions on Plasma Science* **38** 996 ISSN 0093-3813
- [54] Jeong S H, Lee K D, Kogi Y, Kawahata K, Nagayama Y, Mase A and Kwon M 2010 *Review of Scientific Instruments* **81** 10D922
- [55] Lee K C, Juhn J W, Nam Y U, Kim Y S, Wi H M, Kim S W and Ghim Y c 2016 *Fusion Engineering and Design* **113** 87
- [56] Yun G S, Lee W, Choi M J, Lee J, Kim M, Leem J, Nam Y, Choe G H, Park H K, Park H, Woo D S, Kim K W, Domier C W, Luhmann N C, Ito N, Mase A and Lee S G 2014 *Review of Scientific Instruments* **85** 11D820
- [57] Nam Y U, Zoleznik S, Lampert M, Kovacsik A and Wi H M 2014 *Review of Scientific Instruments* **85** 11E434
- [58] Choi M J 2019 <https://arXiv.org/1907.09184v3>
- [59] Lao L L, John H S, Stambaugh R D, Kellman A G and Pfeiffer W 1985 *Nuclear Fusion* **25** 1611
- [60] Choi M J, Yun G S, Lee W, Park H K, Park Y S, Sabbagh S A, Gibson K J, Bowman C, Domier C W, Luhmann N C, Bak J G, Lee S G and Team t K 2014 *Nuclear Fusion* **54** 083010
- [61] Choi M J 2022 *syndia: First release*
- [62] VanderPlas J T 2018 *The Astrophysical Journal Supplement Series* **236** 16
- [63] Ankerst M, Breunig M M, Kriegel H P and Sander J 1999 *ACM SIGMOD Record* **28** 49 ISSN 0163-5808
- [64] Pedregosa F, Varoquaux G, Gramfort A, Michel V, Thirion B, Grisel O, Blondel M, Müller A, Nothman J, Louppe G, Prettenhofer P, Weiss R, Dubourg V, Vanderplas J, Passos A, Cournapeau D, Brucher M, Perrot M and Duchesnay É 2011 *Journal of Machine Learning Research* **12** 2825
- [65] Garbet X, Sarazin Y, Imbeaux F, Ghendrih P, Bourdelle C, Gurcan O D and Diamond P H 2007 *Physics of Plasmas* **14** 122305
- [66] Sauter O, Angioni C and Lin-Liu Y R 1999 *Physics of Plasmas* **6** 2834
- [67] Gurcan O D, Diamond P H, Hahm T S and Lin Z 2005 *Physics of Plasmas* **12** 032303 ISSN 1070-664X
- [68] Pearlstein L D and Berk H L 1969 *Physical Review Letters* **23** 220 ISSN 0031-9007
- [69] Miyamoto K 2007 *Controlled fusion and plasma physics* (Taylor and Francis Group)
- [70] Garbet X, Laurent L, Samain A and Chinardet J 1994 *Nuclear Fusion* **34** 963
- [71] Nazikian R, Shinohara K, Kramer G J, Valeo E, Hill K, Hahm T S, Rewoldt G, Ide S, Koide Y, Oyama Y, Shirai H and Tang W 2005 *Physical Review Letters* **94** 135002
- [72] Inagaki S, Tokuzawa T, Itoh K, Ida K, Itoh S I, Tamura N, Sakakibara S, Kasuya N, Fujisawa A, Kubo S, Shimozuma T, Ido T, Nishimura S, Arakawa H, Kobayashi T, Tanaka K, Nagayama Y, Kawahata K, Sudo S, Yamada H and Komori A 2011 *Physical Review Letters* **107** 115001
- [73] Kin F, Fujisawa A, Itoh K, Kosuga Y, Sasaki M, Inagaki S, Nagashima Y, Yamada T, Kasuya N, Yamasaki K, Hasamada K, Zhang B Y, Kawachi Y, Arakawa H, Kobayashi T and Itoh S I 2019 *Physics of Plasmas* **26** 042306 ISSN 1070-664X
- [74] Kishimoto Y, Imadera K, Ishizawa A, Wang W and Li J Q 2023 *Philosophical Transactions of the Royal Society A* **381** 20210231 ISSN 1364-503X
- [75] Hong R, Rhodes T L, Ren Y, Diamond P H, Jian X, Zeng L, Barada K, Yan Z and McKee G R 2023 *Physics of Plasmas* **30** 072512 (Preprint [2303.00059](https://arXiv.org/2303.00059))
- [76] Jensen E J 1998 *Self-Organized Criticality* (Cambridge University Press) ISBN 0-521-48371-9
- [77] Lee W D, Rice J E, Marmar E S, Greenwald M J, Hutchinson I H and Snipes J A 2003 *Physical Review Letters* **91** 205003 ISSN 0031-9007

- [78] Hughes D W and Brummell N H 2021 *The Astrophysical Journal* **922** 195 ISSN 0004-637X
- [79] Obuse K, Takehiro S i and Yamada M 2010 *Physics of Fluids* **22** 056601 ISSN 1070-6631
- [80] Stephens M A 1974 *Journal of the American Statistical Association* **69** 730 ISSN 0162-1459
- [81] Scholz F W and Stephens M A 1987 *Journal of the American Statistical Association* **82** 918 ISSN 0162-1459
- [82] Milovanov A V, Rasmussen J J and Dif-Pradalier G 2021 *Physical Review E* **103** 052218 ISSN 2470-0045
- [83] Rinne H 2008 *The Weibull Distribution* (London: Chapman and Hall)
- [84] Ku S, Abiteboul J, Diamond P H, Dif-Pradalier G, Kwon J M, Sarazin Y, Hahm T S, Garbet X, Chang C S, Latu G, Yoon E S, Ghendrih P, Yi S, Strugarek A, Solomon W and Grandgirard V 2012 *Nuclear Fusion* **52** 063013
- [85] Gurcan O D and Diamond P H 2015 *Journal of Physics A: Mathematical and Theoretical* **48** 293001 ISSN 1751-8121
- [86] Chung J, Kim H S, Jeon Y M, Kim J, Choi M J, Ko J, Lee K D, Lee H H, Yi S, Kwon J M, Hahn S H, Ko W H, Lee J H and Yoon S W 2017 *Nuclear Fusion* **58** 016019